An Inductive and Capacitive Combined Wireless Power Transfer System With *LC*-Compensated Topology

Fei Lu, *Student Member, IEEE*, Hua Zhang, *Student Member, IEEE*, Heath Hofmann, *Senior Member, IEEE*, and Chunting Chris Mi, *Fellow, IEEE*

***Abstract*—This paper proposes a combined inductive and capacitive wireless power transfer (WPT) system with *LC*-compensated topology for electric vehicle charging application. The circuit topology is a combination of the *LCC*-compensated inductive power transfer (IPT) system and the *LCLC*-compensated capacitive power transfer (CPT) system. The working principle of the combined circuit topology is analyzed in detail, providing the relationship between the circuit parameters and the system power. The design of the inductive and capacitive coupling is implemented by the finite-element analysis. The equivalent circuit model of the coupling plates is derived. A 3.0-kW WPT system is designed and implemented as an example of combined inductive and capacitive coupling. The inductive coupler size is 300 mm $\times$ 300 mm and the capacitive coupler is 610 mm $\times$ 610 mm. The air-gap distance is 150 mm for both couplers. The output power of the combined system is the sum of the IPT and CPT system. The prototype has achieved 2.84-kW output power with 94.5% efficiency at 1-MHz switching frequency, and performs better under misalignment than the IPT System. This demonstrates that the inductive–capacitive combined WPT system is a potential solution to the electric vehicle charging application.**

***Index Terms*—Capacitive power transfer, decoupled-capacitor model, electric field, electric vehicle (EV), high-frequency wireless power transfer, inductive and capacitive combined, inductive power transfer, magnetic field, misalignment ability, resonant circuit, soft-switching condition.**

Manuscript received August 05, 2015; revised October 08, 2015 and December 10, 2015; accepted January 11, 2016. Date of publication January 20, 2016; date of current version July 08, 2016. This work was supported in part by the U.S. Department of Energy Graduate Automotive Technology Education Grant, the U.S.-China Clean Energy Research Center—Clean Vehicle Consortium, DENSO International, San Diego State University, the University of Michigan-Ann Arbor, and China Scholarship Council, and also by the U.S. Department of Energy under Award DE-PI0000012. Recommended for publication by Associate Editor J. M. Rivas Davila.

F. Lu is with the Electrical Engineering and Computer Science Department, University of Michigan, Ann Arbor, MI 48109 USA, and also with Department of Electrical and Computer Engineering, San Diego State University, San Diego, CA 92182 USA (e-mail: feilu@umich.edu).

H. Zhang is with the Department of Electrical and Computer Engineering, San Diego State University, San Diego, CA 92182 USA, and also with the School of Automation, Northwestern Polytechnical University, Xi'an 710072, China (e-mail: huazhang@umich.edu).

H. Hofmann is with the Electrical Engineering and Computer Science Department, University of Michigan, Ann Arbor, MI 48109 USA (e-mail: hofmann@umich.edu).

C. C. Mi is with the Department of Electrical and Computer Engineering, San Diego State University, San Diego, CA 92182 USA (e-mail: cmi@sdsu.edu).

Color versions of one or more of the figures in this paper are available online at http://ieeexplore.ieee.org.

Digital Object Identifier 10.1109/TPEL.2016.2519903

I. Introduction

WIRELESS power transfer technology can be divided into two categories: inductive power transfer (IPT) [1], [2] and capacitive power transfer (CPT) [3], [4]. The IPT system utilizes magnetic fields to transfer power, and the CPT system makes use of electric fields.

The IPT technology has been widely studied in previous research. It consists of two planar coils with an air-gap distance around 150 mm for vehicle charging applications [5]. The two coils form a separated transformer, in which the primary side is loosely coupled with the secondary side [6]. The coupling coefficient between the primary and secondary coil is much smaller than 1.0, and usually in the range of 0.1–0.3. This means that the leakage inductance is significantly larger than the mutual inductance. When it is used as a regular transformer, it cannot transfer high power efficiently. Therefore, a corresponding compensation circuit is necessary to resonate with the coils and provide high voltage at both input and output to transfer high power.

The IPT system can be classified according to the compensation circuit topology. Conventionally, a single capacitor is connected in series or parallel with the coil which results in four topologies, listed as series–series, series–parallel, parallel–series, and parallel–parallel (PP) [7]–[9]. Their advantage is simplicity. However, they are not suitable for all load conditions [10]. When the load varies between light and heavy, they cannot maintain high efficiency. Another problem is that the coil position misalignment could break the resonance between the capacitor and coil, which in turn can cause power dramatically drop or increase.

The double-sided *LCC*-compensated topology is a better solution to compensate the power-transmitting coils, in which one external inductor and two external capacitors are required at each side [11]. With this topology, the resonant tank acts as a current source to both the input and output, which means the output current is independent of the load condition. In the battery charging application, the resonant circuit is, therefore, not affected by the battery voltage variation. Therefore, it is suitable to provide constant current charging condition to the batteries. Another benefit of *LCC* topology is that it can provide nearly unity power factor to the input side inverter, so there is almost no reactive power injected into the resonant tank, which results in high efficiency for this topology. In [12], a *LCC*-compensated system has achieved 96% efficiency at 7-kW output power, and

the total grid-to-battery efficiency of the wireless charger can achieve 93%. It is already comparable with the traditional wire-connected charger with *LLC* resonant converter [13]. Moreover, this topology compensates using the self-inductance of the coils, which is independent of misalignment. Therefore, the resonance is maintained even in large misalignment cases. Although more components are used in this compensation circuit, the two external inductors can be integrated into the main coils to save space and make the system more compact [14]–[16].

Compared to the IPT technology, the CPT technology has not been well studied. Especially in the electric vehicle charging area, the CPT system has only recently been applied. Most of the present CPT systems were designed for low-power applications, including USB devices, lamps, and small robots [17]–[20]. The transmitted distance in these applications is limited to the millimeter range and the power is lower than tens of watts.

When two metal plates are separated by an air-gap distance of 150 mm, the capacitance is small (e.g., tens of picofarad), which requires a very large inductance value (e.g., millihenry) or very high switching frequency (e.g., tens of megahertz) to provide resonant conditions to the capacitor. However, a large inductor is difficult to make, and its parasitic resistance can dramatically reduce the system efficiency. Also, too high of a switching frequency is also difficult to achieve in practice, and the power level of a high-frequency converter is usually limited to hundreds of watts [21]. Also, the CPT approach requires high electric fields to transfer high power, which can result in significant safety concerns to the general public [22].

The CPT system is classified according to the compensation circuit topology. Similar to the IPT system, the most widely used topology in CPT systems is a single inductor connected in series with the coupling capacitor to form a series resonance. However, this topology has only been used with large capacitances, where the inductance and switching frequency are reasonable [23]–[26]. Another topology is the class-E converter, in which the coupling capacitor works as a regular resonant component [27], [28]. However, its efficiency and power are limited by the high-frequency converter. A high-frequency PWM converter has been used to realize capacitive power transfer [29], [30]. However, it requires the capacitance value to be in the tens of nanofarad range, and the distance is less than 1 mm. Current CPT systems have achieved 1-kW power transfer and 90% efficiency. They have been designed for stationary charging with the charging gap in the millimeter range, and also have good field confinement [31].

The double-sided *LCLC* compensated topology has been proposed in [32], in which two external inductors and two external capacitors are used on each side of the coupling capacitor. Compared with previous work, this system has the potential to be applied to mobile charging of an electric vehicle, but generates significant leakage electric field emissions due to the large air-gap distance. The system has achieved 2.4-kW power transfer through an air-gap distance of 150 mm at 90.8% efficiency with two pairs of 610 mm $\times$ 610 mm aluminum plates. The system also has good performance with large misalignment and air-gap variation. At 300-mm misalignment, the output power is 2.1 kW with 90.7% efficiency. At 300-mm air-gap distance, the output power is 1.6 kW with 89.1% efficiency. It proves that the *LCLC* topology is a good candidate to realize capacitive charging for electric vehicles.

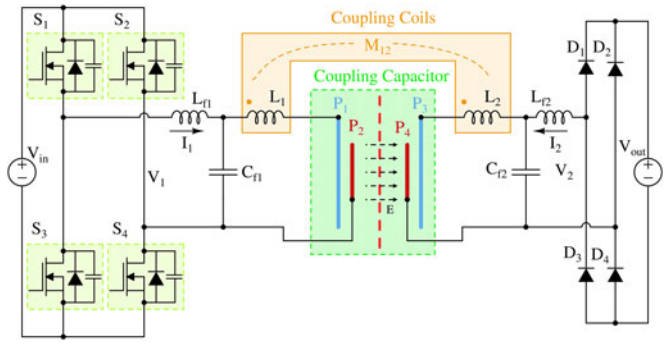

Fig. 1. Circuit topology of the *LC*-compensated IPT-CPT system.

Comparing the circuit topologies of *LCC*-IPT system and *LCLC*-CPT system, it is meaningful to reduce the external component number and simplify the circuit design. Therefore, they can be combined together to make full use of the coupling coils and metal plates, which results in an *LC*-compensated IPT-CPT combined system. The coupling coils work as the IPT components, as well as the inductors resonating with the coupling metal plates. The coupling metal plates work as the capacitive power transferring components, as well as the capacitors resonating with the coupling coils. The circuit topology is shown in Fig. 1. This system takes full advantages of the electric and magnetic fields in the resonant circuit.

II. Circuit Topology and Working Principle

A. LC Compensated IPT-CPT Topology

The corresponding IPT-CPT system topology is shown in Fig. 1. The primary and secondary sides are separated by a red dashed line. It is similar with the CPT system proposed in reference [32], except that two of the inductors L_1 and L_2 are coupled to transfer power from the primary side to the secondary side using magnetic fields. At each side, there are only two external components connected to the coupling coils and capacitors.

For the coupling coils, it is similar to the regular IPT system. However, it is important to pay attention to the coupling polarity of L_1 and L_2. The connection in Fig. 1 can result in an addition of the inductive power with the capacitive power. If the coupling polarity is reversed, the two types of power transfer will cancel. The coil design process will be analyzed in details in Section III-A.

For the coupling capacitors, the four plates are arranged as shown in Fig. 5. The equivalent circuit model is derived in Section III-B, which contains two small capacitances, $C_{s1,2}$, and two large capacitances, $C_{1,2}$. Compared to [32], no external capacitor is connected with the coupling capacitors, and the system structure is further simplified. The coupling capacitors design process will also be presented in Section III-B.

An H-bridge MOSFET inverter is used at the input side and an H-bridge diode rectifier is connected at the output side to the

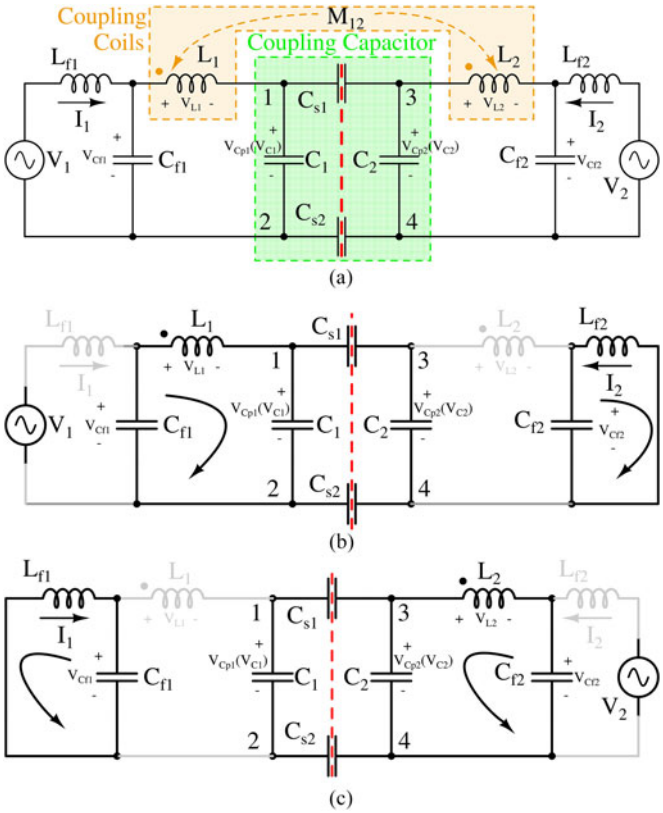

Fig. 2. FHA analysis. (a) Simplified resonant circuit topology. (b) Components excited by the input voltage. (c) Components excited by the output voltage.

load. Silicon carbide (SiC) MOSFETs (C2M0080120D) from CREE are used in the inverter. The circuit in Fig. 1 can be tuned to provide soft-switching conditions to the inverter to mitigate the switching losses. In the rectifier, SiC diodes (IDW30G65C5) from Infineon are applied.

B. Circuit Working Principle

The input-side inverter generates a square-wave voltage excitation, and injects power into the resonant tank. The output-side rectifier converts the output ac current into dc form and supplies the battery. Therefore, both the input and output voltage contain high-order harmonic components. However, the *LC* compensation network serves as low-pass filter; therefore, the fundamental harmonics approximation (FHA) can be used to analyze working principle, as shown in Fig. 2.

Fig. 2(a) shows the simplified resonant circuit topology of Fig. 1. The coupling capacitor is replaced by the equivalent circuit model in Fig. 6, which will be presented in Section III-B. The input and output are replaced by two sinusoidal voltage sources. The superposition theorem is used to divide the two-source circuit into two single-source linear circuits, as shown in Fig. 2(b) and (c), respectively.

Fig. 2(b) shows the components excited only by the input voltage source at the design frequency. There are two parallel resonances highlighted in Fig. 2(b). The components in gray conduct no current, so they can be treated as an open circuit. The circuit in Fig. 2(b) results in the following equations:

$$\begin{cases} \omega = 2\pi \cdot f_{\mathrm{sw}} \\ C_s = \dfrac{1}{1/C_{s1} + 1/C_{s2}} \\ C_{p1} = C_1 + \dfrac{1}{1/C_s + 1/C_2} \\ \omega = 1/\sqrt{L_{f2} \cdot C_{f2}} \\ \omega = 1/\sqrt{L_1 \cdot \dfrac{1}{1/C_{p1} + 1/C_{f1}}} \end{cases} \tag{1}$$

where the switching frequency is f_{sw}, and C_{p1} is the input capacitance of the coupling capacitor from the primary side. Equation (1) shows that L_{f2} and C_{f2} form a parallel resonance, and the impedance is infinite. There is no current flow through the inductor L_2. Also, L_1, C_{f1}, and C_{p1} form another parallel resonance. There is no current flow through the inductor L_{f1}. The current on L_{f1} is also the input current to the resonant tank. So, the input current is independent of the input voltage, which means the circuit can work as a current source to the input.

Fig. 2(c) shows the components excited only by the output voltage source at the desired frequency. There are two parallel resonances highlighted in Fig. 2(c). The relationship between components is expressed as

$$\begin{cases} C_{p2} = C_2 + \dfrac{1}{1/C_s + 1/C_1} \\ \omega = 1/\sqrt{L_{f1} \cdot C_{f1}} \\ \omega = 1/\sqrt{L_2 \cdot \dfrac{1}{1/C_{p2} + 1/C_{f2}}} \end{cases} \tag{2}$$

where C_{p2} is the input capacitance of the coupling capacitor from the secondary side. Equation (2) shows that L_{f1} and C_{f1} form a parallel resonance. L_2, C_{f2}, and C_{p2} form another parallel resonance. There is no current flow through inductors L_1 and L_{f2}. The current on L_{f2} is also the output current to the load. The output current is therefore independent of the output voltage, and the resonant circuit works as a current source to the output.

C. System Power Calculation

First, the circuit in Fig. 2(b) is used to calculate the output current and output power. It needs to be emphasized again that the output current only depends on the input voltage, as shown in Fig. 2(b). The input voltage V_1 is set to be the reference phasor in the following analysis.

The parallel resonance of L_f, C_{f1}, and C_{p1} is considered, so the voltage on each component can be expressed as

$$\begin{cases} V_{\mathrm{Cf1}} = V_1 \\ V_{L1} = \dfrac{j\omega L_1 \cdot V_1}{j\omega L_1 + 1/(j\omega C_{p1})} = \dfrac{j\omega L_1 \cdot V_1}{-1/(j\omega C_{f1})} = \omega^2 L_1 C_{f1} V_1 \\ V_{\mathrm{Cp1}} = \dfrac{1/(j\omega C_{p1}) \cdot V_1}{j\omega L_1 + 1/(j\omega C_{p1})} = \dfrac{1/(j\omega C_{p1}) \cdot V_1}{-1/(j\omega C_{f1})} = \dfrac{-C_{f1}}{C_{p1}} V_1. \end{cases} \tag{3}$$

The voltage on C_{p1} is also the voltage on the capacitor C_1. So the voltage on C_2 can be expressed as

$$V_{c2} = \frac{1/C_2}{1/C_s + 1/C_2} \cdot V_{C1} = \frac{1/C_2}{1/C_s + 1/C_2} \cdot \frac{-C_{f1}}{C_{p1}} \cdot V_1. \tag{4}$$

Considering the expression (1), the voltage on C_2 can be further simplified as

$$V_{c2} = \frac{-C_s \cdot C_{f1}}{C_1C_s + C_2C_s + C_1C_2} \cdot V_1. \tag{5}$$

Since L_1 and L_2 are magnetically coupled and there is current flow through L_1, there is also a voltage difference between the two terminals of L_2. The dot end connection in Fig 2(b) determines the direction of this voltage. So the voltage on L_2 can be expressed as

$$V_{L2} = \frac{M_{12}}{L_1} \cdot V_{L1} = \omega^2 M_{12} C_{f1} V_1. \tag{6}$$

M_{12} is the mutual inductance, which is written as

$$M_{12} = k\sqrt{L_1 \cdot L_2} \tag{7}$$

where k is the coupling coefficient. With the expression of (5) and (6), the voltage on C_{f2} can be expressed as

$$V_{\mathrm{Cf2}} = V_{C2} - V_{L2} = \frac{-C_s \cdot C_{f1} \cdot V_1}{C_1C_s + C_2C_s + C_1C_2} - \omega^2 M_{12} C_{f1} V_1. \tag{8}$$

Equation (8) indicates that the polarity connection of L_2 has to be the same as shown in Fig. 2(b). Otherwise, the voltage V_{C2} and V_{L2} will be canceled, and the output power is, therefore, reduced.

The voltage on C_{f2} is the same as the voltage on L_{f2}, so the output side current I_2 can be expressed as

$$I_2 = \frac{-V_{C_{f2}}}{j\omega L_{f2}} = \frac{C_s \cdot C_{f1} \cdot V_1/(j\omega L_{f2})}{C_1C_s + C_2C_s + C_1C_2} + \frac{\omega^2 M_{12} C_{f1} V_1}{j\omega L_{f2}}. \tag{9}$$

Considering the parallel resonance between L_{f2} and C_{f2} and the expression (1), (9) can be simplified as

$$I_2 = \frac{-j\omega C_s \cdot C_{f1} C_{f2} \cdot V_1}{C_1C_s + C_2C_s + C_1C_2} + \frac{-jM_{12} \cdot V_1}{\omega L_{f1} L_{f2}}. \tag{10}$$

As an H-bridge diode rectifier is used in Fig. 1 at the output side, the fundamental output current ($-I_2$) and output voltage V_2 are in phase with each other. Therefore, the output power can be expressed as

$$P_{\mathrm{out}} = |V_2| \cdot |(-I_2)| = \frac{\omega C_s \cdot C_{f1} C_{f2} |V_1| |V_2|}{C_1C_s + C_2C_s + C_1C_2} + \frac{M_{12} |V_1| |V_2|}{\omega L_{f1} L_{f2}}. \tag{11}$$

In expression (11), the first term is determined by the capacitive power transfer, and the second term is determined by the IPT

$$\begin{cases} P_{\mathrm{CPT}} = \dfrac{\omega C_s \cdot C_{f1} C_{f2} \cdot |V_1| \cdot |V_2|}{C_1C_s + C_2C_s + C_1C_2} \\ P_{\mathrm{IPT}} = \dfrac{M_{12} \cdot |V_1| \cdot |V_2|}{\omega L_{f1} L_{f2}} \end{cases}. \tag{12}$$

Equation (10) indicates that the output current ($-I_2$) leads the input voltage V_1 by 90°. In the H-bridge diode rectifier, the output current ($-I_2$) and the output voltage V_2 are in phase. Therefore, the output voltage V_2 is leading the input voltage V_1 by 90°.

Second, Fig. 2(c) is used to calculate the input current and input power. It needs to be emphasized again that the input current only depends on the output voltage as shown in Fig. 2(c). Similarly to the previous analysis, the input current I_1 can be expressed as

$$I_1 = \frac{-V_{C_{f1}}}{j\omega L_{f1}} = \frac{-j\omega C_s \cdot C_{f1} C_{f2} \cdot V_2}{C_1C_s + C_2C_s + C_1C_2} + \frac{-jM_{12} V_2}{\omega L_{f1} L_{f2}}. \tag{13}$$

This equation shows that the output voltage V_2 is leading the input current I_1 by 90°. Since the previous analysis proves that the output voltage V_2 is also leading the input voltage V_1 by 90°, the input voltage V_1 and current I_1 are in phase with each other. Therefore, the input power can be expressed as

$$P_{\mathrm{in}} = |V_1| \cdot |I_1| \cdot \cos(\varphi_{V_1} - \varphi_{I_1}) = |V_1| \cdot |I_1|. \tag{14}$$

Expression (15) shows that unity power factor is realized at the input side and there is no reactive power injected into the resonant tank. Therefore, there is no extra conduction loss induced by the circulating reactive current, and the efficiency of the resonant circuit can be very high.

Combining (13) and (14), the input power is further expressed as

$$P_{\mathrm{in}} = |V_1| \cdot |I_1| = \frac{\omega C_s \cdot C_{f1} C_{f2} \cdot |V_1| |V_2|}{C_1C_s + C_2C_s + C_1C_2} + \frac{M_{12} \cdot |V_1| |V_2|}{\omega L_{f1} L_{f2}}. \tag{15}$$

Comparing (11) and (15), it shows that the input power is the same as the output power, which is consistent with the previous assumption that the losses in all the components are neglected. According to Dai and D.C. Ludois [30], the relationship between C_1, C_2, and C_s satisfies $C_1 \gg C_s$ and $C_2 \gg C_s$. So (11) and (15) can be further simplified as

$$P_{\mathrm{in}} = P_{\mathrm{out}} \approx \omega C_s \cdot \frac{C_{f1} C_{f2}}{C_1 C_2} \cdot |V_1| |V_2| + \frac{k\sqrt{L_1 L_2}}{\omega L_{f1} L_{f2}} \cdot |V_1| |V_2|. \tag{16}$$

III. Inductive and Capacitive Coupler Design

A. Inductive Coupler Design

The switching frequency needs to be specified at the beginning of the coupler design. From (12), P_{CPT} is proportional to the coupling capacitor C_s, which is usually in the picofarad range, so the switching frequency has to be increased to the MHz level to achieve the desired power transfer by the capacitors. Since the inductive couplers (coils) share the same frequency as the capacitive couplers (plates), the switching frequency should be limited to reduce the skin effect. As a result, the frequency is set to 1 MHz.

The contribution of this paper mainly lies in the validation of the IPT-CPT combined system. For simplicity, shielding of the leakage magnetic field is not considered in the coil design. According to a previous study, the ferrite and aluminum plate

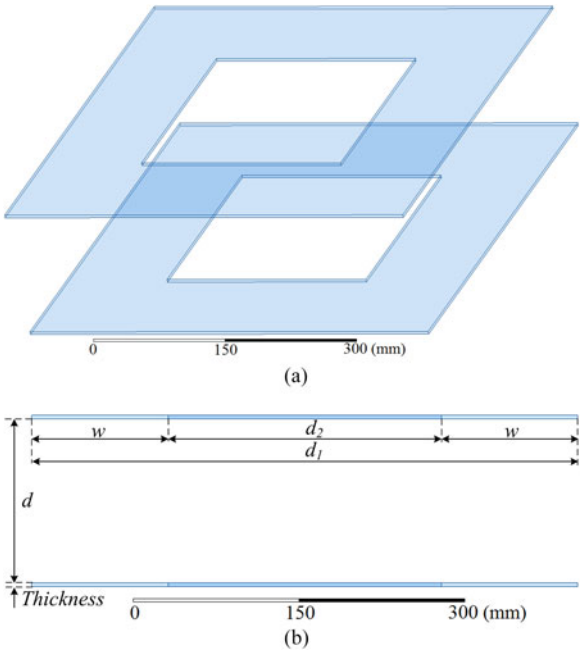

Fig. 3. Dimension of the coils. (a) 3-D view of the coils. (b) Front view of the coils.

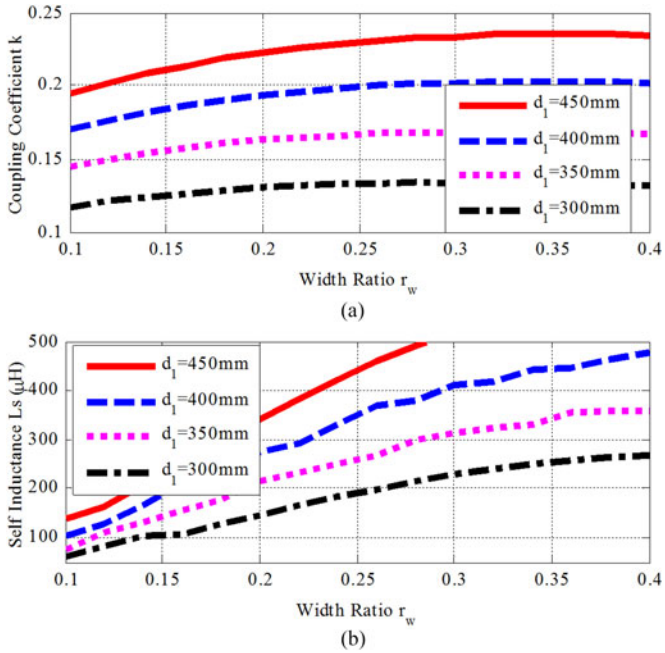

Fig. 4. Maxwell simulation of the coupling coefficient and self-inductance. (a) Coupling coefficient at different dimensions. (b) Self-inductance at different dimensions.

can be used together to shield the leakage field and they will incur 1%–3% extra loss, depending on the structure [33].

The dimension of the coil is shown in Fig. 3(a) and (b), where d_1 is the outer length of the coil, d_2 is the inner length, d is the air gap, and w is the coil width. The width ratio is defined as $r_w = w/d_1$. The coil has a square shape, and the air-gap distance is 150 mm. The coil thickness has a little effect on the coupling coefficient, and is determined by the Litz-wire diameter. In this case, the thickness is 3.2 mm.

The coupling coefficient k and self-inductance L_s of the coils are simulated in Maxwell, and shown in Fig. 4(a) and (b). Fig. 4(a) indicates that the coupling coefficient k is mostly determined by the coil outer length d_1. When d_1 is between 300 to 450 mm, k is in the range of 0.1 to 0.25. Fig. 4(b) shows that the self-inductance L_s can be regulated by varying the width ratio r_w without affecting coupling coefficient.

In the IPT-CPT combined system, the coils resonate with the metal plates. Therefore, the coil size cannot be decided without considering the dimension of the plates. The balancing of the output power of the IPT and CPT system is also an important specification. The coil dimensions will be determined in Section IV, where a specific 3.0-kW design example is provided.

B. Capacitive Coupler Design

Four metal plates are used to form capacitors to transfer power through electric fields, and they are separated into two pairs at the primary and secondary. The structure of the capacitive coupler is shown in Fig. 5, where l_1 is the length of the outer plate, l_2 is the length of the inner plate, d_c is the distance between the inner and outer plate, and d is the air-gap distance same as the inductive coupler. The plate thickness is set to be 2 mm.

The circuit model of the plate is shown in Fig. 6. To simplify the design process, the coupler is symmetric with respect to the primary and secondary sides. All six mutual capacitances between each two plates are illustrated in Fig. 6. Because of the symmetry, $C_{12} = C_{34}$ and $C_{14} = C_{23}$. In the equivalent circuit, $C_1 = C_2$. It needs to be emphasized that C_{13} and C_{24} do not have to be equal; the same for C_{s1} and C_{s2}. The nodal voltage method can be used to derive the relationship between the original model and the equivalent model. The equivalent model is used in Section II-B.

For the plates, there are three parameters that need to be determined: l_1, l_2, and d_c. In this design, the outer plate length is set to be 610 mm due to the space limitation. The other two parameters, l_2 and d_c, are varied to find the best dimensions. All the mutual capacitances can be obtained from Maxwell and converted to equivalent parameters. The plate ratio r_p is defined as $r_p = l_2/l_1$. The capacitances $C_s = C_{s1}C_{s2}/(C_{s1} + C_{s2})$ and $C_{1,2}$ are shown in Fig. 7. This figure indicates that C_s is not highly sensitive to the plate distance d_c.

The plate ratio is set to 0.75 to maximize the coupling capacitance. The parameter d_c is, therefore, the only parameter that needs to be determined. It is used to determine the capacitances $C_{1,2}$, and, hence, the resonance with the inductive coils. In Section IV, the distance d_c will be determined in a 3.0-kW design example.

IV. 3.0-kW Example for EV Charging

A. Power Ratio of the IPT and CPT System

This system utilizes both inductive and capacitive coupling to transfer power. It is important to determine the power ratio of each part, which is the percentage of their contributions. Since

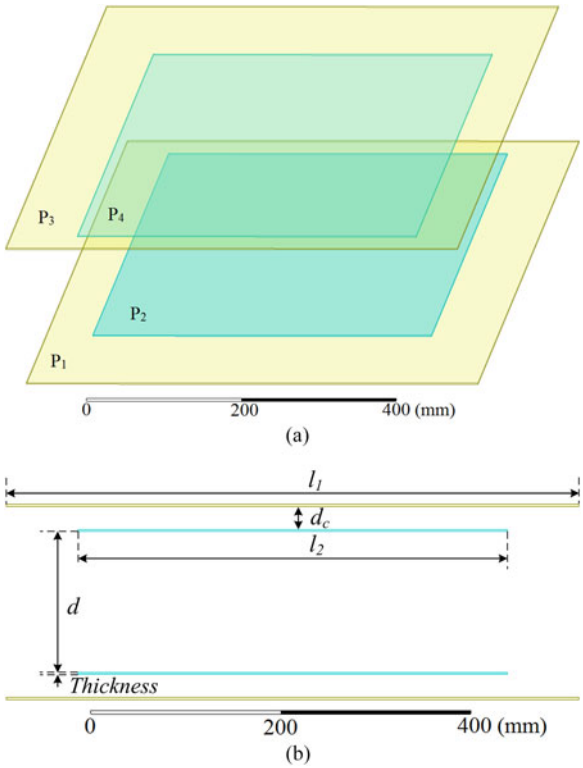

Fig. 5. Dimension of the plates. (a) 3-D view of the plates. (b) Front view of the Plates.

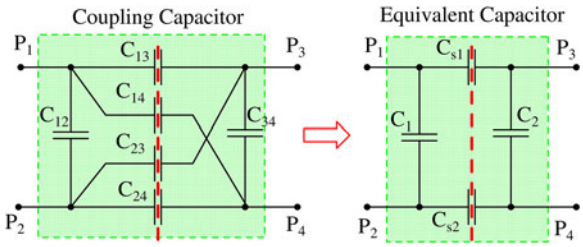

Fig. 6. Circuit model of the plates.

the IPT and CPT coupler have similar physical size, they can be designed to transfer the same order of magnitude of power to the load. According to (1), the power ratio of inductive power to capacitive power can be defined as

$$r_{I-C} = \frac{P_{\mathrm{IPT}}}{P_{\mathrm{CPT}}} = \frac{M_{12} \cdot (C_1C_s + C_2C_s + C_1C_2)}{\omega L_{f1}L_{f2} \cdot \omega C_s \cdot C_{f1}C_{f2}}. \quad (17)$$

Considering (1), (2), and (7), (17) can be simplified as

$$r_{I-C} = \frac{P_{\mathrm{IPT}}}{P_{\mathrm{CPT}}} = \frac{\omega^2 k\sqrt{L_1L_2} \cdot (C_1C_s + C_2C_s + C_1C_2)}{C_s}. \quad (18)$$

Since $L_1 = L_2$ and $C_1 = C_2$, (18) can be further rewritten:

$$r_{I-C} = \frac{P_{\mathrm{IPT}}}{P_{\mathrm{CPT}}} = \frac{\omega^2 k \cdot L_1C_1(2C_s + C_1)}{C_s} \quad (19)$$

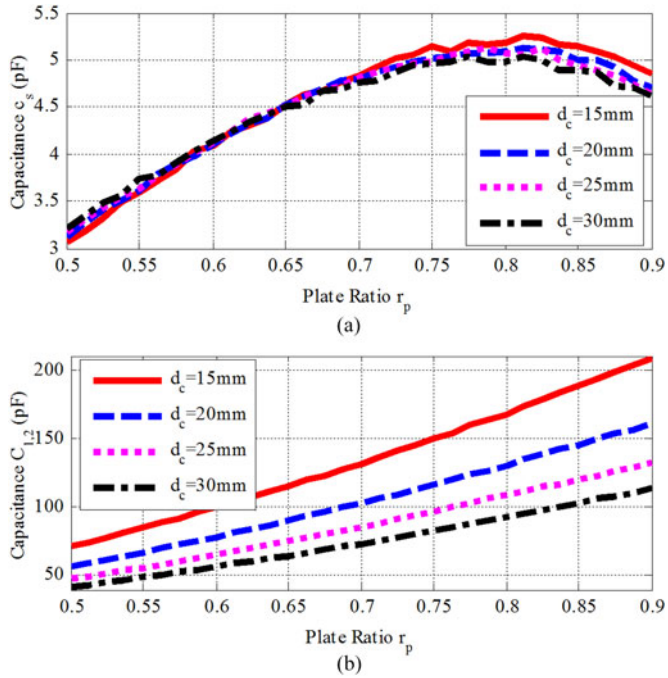

Fig. 7. Capacitances at r_p and d_c when $l_1 = 610$ mm. (a) Capacitance C_s. (b) Capacitance $C_{1,2}$.

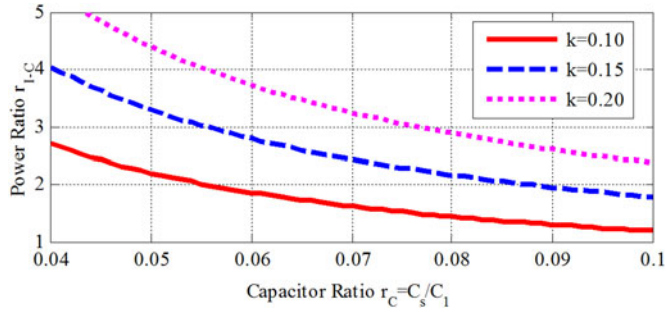

Fig. 8. Power ratio between the IPT and CPT system.

Since L_1, C_{f1}, and C_{p1} form a parallel resonance, the inductor L_1 can be replaced by the capacitor C_{f1} and C_{p1}

$$r_{I-C} = \frac{P_{\mathrm{IPT}}}{P_{\mathrm{CPT}}} = k \cdot \frac{C_1}{C_s} \cdot \frac{C_1 + 2C_s}{C_1 + C_sC_s/(C_1 + C_s)} \frac{C_{p1} + C_{f1}}{C_{f1}}. \quad (20)$$

Referring to [32], it is known that $C_{f1} \gg C_{p1}$, so (20) is approximated as

$$r_{I-C} = \frac{P_{\mathrm{IPT}}}{P_{\mathrm{CPT}}} \approx k \cdot \frac{C_1}{C_s} \cdot \frac{C_1 + 2C_s}{C_1 + C_sC_s/(C_1 + C_s)}. \quad (21)$$

The capacitor ratio between C_1 and C_s can be defined as $k_C = C_s/C_1$. Therefore, the power ratio can be written as

$$r_{I-C} = \frac{P_{\mathrm{IPT}}}{P_{\mathrm{CPT}}} \approx \frac{k}{k_C} \cdot \frac{1 + 2 \cdot k_C}{1 + k_C^2/(1 + k_C)}. \quad (22)$$

Fig. 4(a) shows that the coupling coefficient k varies from 0.10 to 0.20, and Fig. 7 shows that the capacitor ratio k_c varies from 0.04 to 0.10. Therefore, the power ratio between the IPT and CPT system is shown in Fig. 8, in which the IPT system contributes more to the output power.

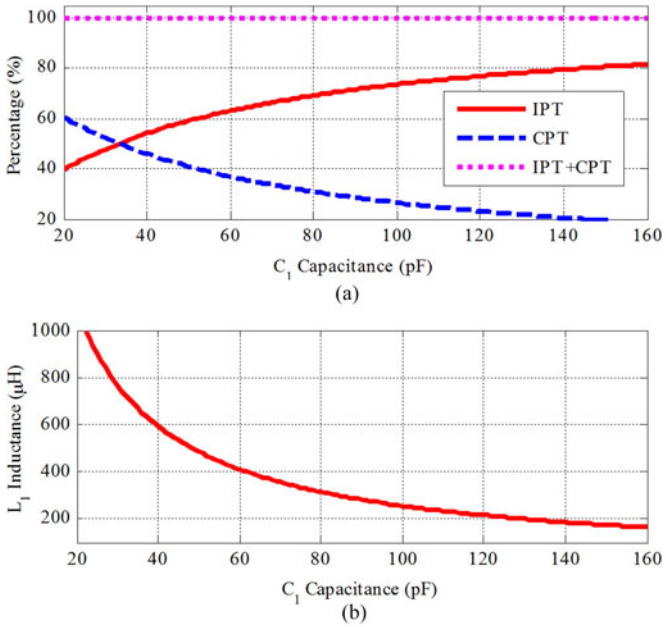

Fig. 9. Parameter relationship in a 3.0-kW Example. (a) C_1 versus IPT/CPT power percentage. (b) C_1 versus L_1 value.

TABLE I
SYSTEM SPECIFICATIONS AND CIRCUIT PARAMETERS

Parameter	Design Value	Parameter	Design Value
$V_{\rm in}$	310 V	$V_{\rm out}$	320 V
$P_{\rm IPT}$	2160 W (72%)	$P_{\rm CPT}$	840 W (28%)
d_1	300 mm	l_1	610 mm
d_2	90 mm	l_2	457 mm
d	150 mm	d_c	25 mm
r_w	0.35	r_p	0.75
k	0.130	k_c	0.052
$f_{\rm sw}$	1 MHz	C_s	5.0 pF
L_{f1}	14.2 μH	L_{f2}	14.2 μH
C_{f1}	1.78 nF	C_{f2}	1.78 nF
L_1	256.2 μH	L_2	264.1 μH
C_1	96.1 pF	C_2	96.1 pF

B. System Parameter Design

In order to get significant power transfer through CPT coupling, the maximum power ratio is set to be 3.0. The coil length is set to be 300 mm and the coupling coefficient is 0.130. Fig. 7 shows that C_s is around 5.0 pF. In a 3.0-kW system, the input voltage is 310$V_{\rm dc}$ and output voltage is 320 $V_{\rm dc}$. Substitution of $V_{\rm in}$, $V_{\rm out}$, k, C_s, and $P_{\rm in}$ into (1), (2), (15), and (20), shows that C_1 determines the percentage contribution of IPT and CPT, and also the inductance value L_1, as shown in Fig. 9. Considering the space limitation for the coil, its inductance L_1 cannot be too large, so the minimum power ratio is set at 2.0. Therefore, the acceptable power ratio is between 2.0 and 3.0.

The plate distance d_c is set to be 25 mm and $C_1 = 96.1$ pF. Fig. 9(b) indicates that $L_1 = 264.1$ μH, which corresponds to $r_w = 0.35$. Fig. 9(a) shows that the IPT system provides 72% of the total power and the CPT system provides 28%. The designed system specifications and parameters are shown in Table I. L_1 is 7% smaller than L_2 to provide soft-switching conditions [11].

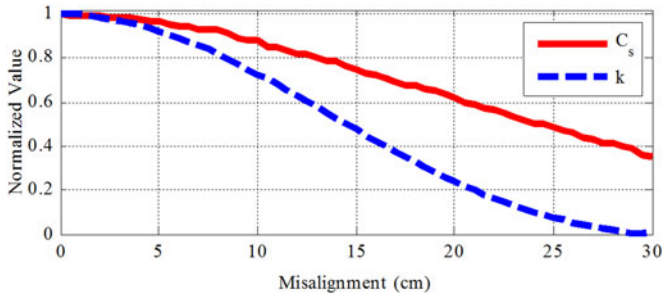

Fig. 10. Normalized values of C_s and k at different misalignments.

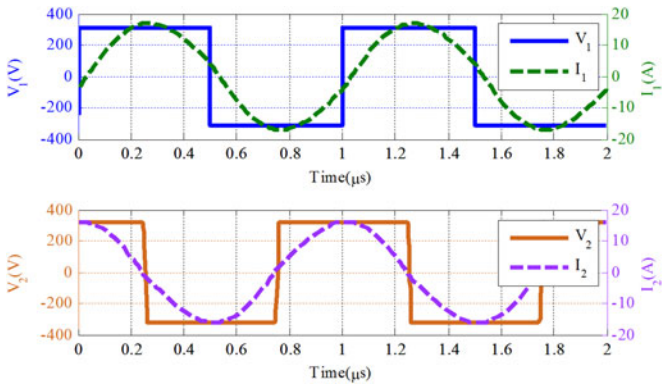

Fig. 11. Simulated input and output voltage and current waveforms.

With the dimensions in Table I, the FEA analysis of the two couplers are conducted at different misalignment conditions. For the capacitive coupler, the variations of $C_{1,2}$ are within 3% when the misalignemnt increases to 30 cm, so only the variation of C_s is considered. For the inductive coupler, the variation of $L_{1,2}$ are within 2%, so only the variation of coupling coeffcient k is considered. The normalized values of coupling capacitor C_s and inductive coupling coeffcient k at different misalignment conditions are shown in Fig. 10. It shows that, in this system, the capacitive coupler has better misalignment ability than the inductive coupler.

LTspice is used to simulate the system input and output power and waveform, as shown in Fig. 11. The voltage and currrent are almost in phase with each other at both the input and output, which is consistent with the analysis in Section II. Also, the cut off current at the switching transient is 3 A to provide soft switching.

LTspice simulation also provides the voltage stress between the metal plates. The RMS voltage between P_1 and P_2 is 4.9 kV, and the RMS voltage between P_1 and P_3 is 3.4 kV. The breakdown voltage of dry air is 3.0 kV/mm and the distance between P_1 and P_2 is 25 mm, so there is no concern with arcing.

The magnetic field distribution of the inductive coupler is shown in Fig. 12(a), and the electric field distribution of the capacitive coupler is shown in Fig. 12(b).

According to the ICNIRP 2010, the safety exposure limit for the general public to magnetic fields is 6.25 μT [34]. In our setups, an aluminum shield was not used. The simulation result in Fig. 12(a) shows that the safe range is 600 mm away from

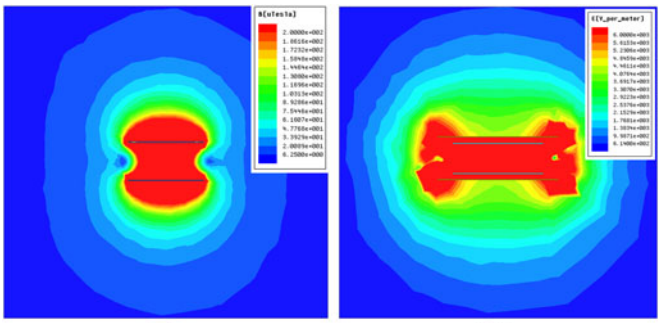

Fig. 12. Fields distribution of the coupler. (a) Magnetic field distribution. (b) Electric field distribution.

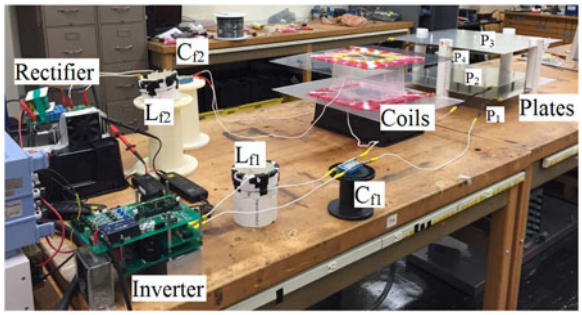

Fig. 13. Experiment prototype of a 3.0-kW *LC*-compensated IPT-CPT System.

the magnetic coupler. In the future, if aluminum shielding is utilized, the magnetic radiation can be significantly reduced.

According to the IEEE C95.1 standard, the safety limit for electric fields is 614 V/m [35]. Fig. 12(b) shows that the safe range is 700 mm away from the coupler. In the future, more research will be conducted to either reduce or shield the electric field radiation.

V. Experimental Details

A. Experimental Setup

A 3.0-kW experiment prototype is constructed to verify the proposed system, which is shown in Fig. 13. All the components are implemented using the values in Table I. The inductors and coils are made by 3000-strand AWG 46 Litz-wire with a single wire diameter of 39.8 μm. Since the skin depth of copper is 65.2 μm at 1 MHz, there is no significant increase of ac resistance induced by the skin effect. However, according to Lu *et al.* [36], the proximity effect between bundles in the Litz-wire cannot be neglected, and the measurement by Agilent LCR meter E4980A shows that the ac resistance is 3.4 times the dc resistance at 1 MHz. The inductors have an air core, and are wound on PVC tubes to eliminate the magnetic losses. The coils are wound on plastic board and there is no magnetic material, as presented in Section III-A. The insulation between the adjacent turns in the coils and inductors should be considered to avoid voltage breakdown. In future designs, the high-frequency magnetic material 51 from Fair-Rite will be used in the inductors and coils to reduce their volume as well as magnetic fields radiation.

High-frequency thin-film capacitors from KEMET are used to realize the compensation capacitors C_{f1} and C_{f2}. At 1 MHz, the RMS voltage rating of a single capacitor is about 300 V, and the RMS current rating of a single capacitor is about 1.0 A. Therefore, multiple capacitors are connected in series and parallel to satisfy the voltage and current requirements. According to the datasheet, the capacitance values have $\pm 5.0\%$ tolerance from the nominal value. To maintain the accuracy of the capacitance values, they are measured and tuned by the Agilent Network Analyze E5072B. The dissipation factor of the capacitors is 18×10^{-4} at 1 MHz, which is used to calculate the equivalent series resistance of the capacitors.

Aluminum plates are used to construct the capacitive couplers. The outer plate length is 610 mm, and the inner plate length is 457 mm. The distance between the outer and inner plates is 25 mm, and the thickness of the plates is 2 mm. PVC tubes are used to hold the plates. The plates are clamped into slots on the tubes, and it is convenient to move the plates in the slots to adjust the misalignment. Since there is high voltage stress between the plates, ceramic spacers are used to separate the outer and inner plate at the same side. In this design, the other circuit components are connected to the edge of the plates, which influences the current distribution in the plates. In future research, the connection of the plates and its influence on efficiency will be studied.

SiC MOSFETs (C2M0080120D) are used in the input inverter, and SiC diodes (IDW30G65C5) are used in the output rectifier, as mentioned in Section II-A. The digital signal processor TMS320F28335 is used to generate the PWM signals for the inverter. It is convenient to adjust the switching frequency and dead-time of the signals in the programming codes. The datasheet shows that the parasitic capacitor between the drain and source of the MOSFET is only 100 pF at 310 V, so it is easy to charge and discharge this capacitor during the switching transient. The MOSFETs in the inverter can therefore achieve soft-switching conditions.

In Fig. 13, the distance between the inductive and capacitive coupler is 300 mm to eliminate the influence between them. If the two couplers are placed close to each other, it can induce some drawbacks. There are capacitive couplings between the coils and plates, and so the equivalent capacitance between the plates can be changed by the proximity of the coils. As a result, the resonances in the circuit can be changed. Also, the magnetic fields of the coils can generate eddy current losses in the metal plates, which can reduce the coil inductance and hence system efficiency. However, the long distance between the two couplers will decrease the power transfer density. In future research, the two couplers will be integrated as a single coupler to increase the power density. In this case, the interaction between the coils and plates will be presented in detail.

B. Experimental Results

The experiment is conducted with the designed prototype. The input dc source voltage is 310 V, and the electronic dc load works at constant 320 V to simulate the battery pack on the vehicle. The experimental waveforms are shown in Fig. 14.

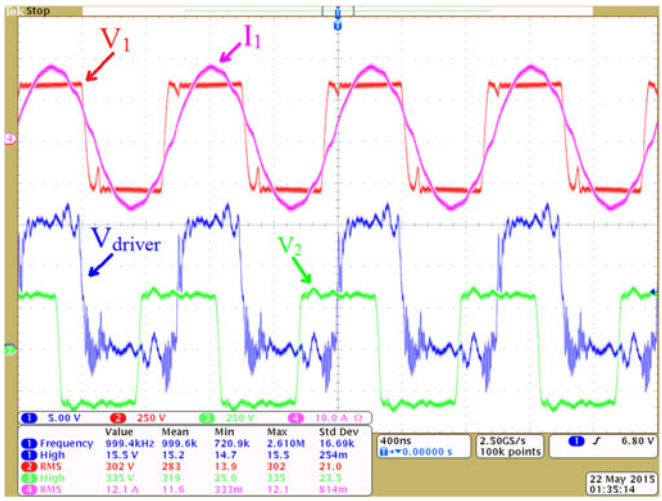

Fig. 14. Experimental input and output waveforms.

In Fig. 14, the red curve is the square wave input voltage V_1 provided by the inverter, and the pink curve is the sinusoidal current I_1 injected into the resonant tank. The green curve is the output square wave voltage V_2 to the rectifier, and the blue curve is the driver signal to one of the MOSFETs. It shows that the input voltage and current are almost in phase, so the system achieves unity power factor. There is little reactive power injected into the circuit, and the efficiency is maintained. The output voltage V_2 is 90° leading the input V_1, which agrees with the analysis in Section II-C. Although there is noise in the driver signal, its magnitude is within 3 V, which is lower than the threshold voltage of MOSFETs. Therefore, it is safe to use this signal as driver.

Fig. 15(a) shows the relationship between the output power and efficiency of the IPT and CPT combined system. In the well-aligned case, the output power reaches a maximum of 2.84 kW with an efficiency of 94.45%. When both the inductive and capacitive couplers have 20-cm misalignment, the output power drops to 1.35 kW, and the efficiency drops to 91.49%.

Fig. 15(b) shows the output power and efficiency of the IPT system. In this case, the two pairs of plates are separated far away to eliminate the capacitive coupling. Only the coils are used to transfer power. When the coils are well aligned, the maximum output power is 1.95 kW with an efficiency of 94.89%. When the coils have 20-cm misalignment, the output power is 0.75 kW, and the efficiency drops to 91.68%.

Fig. 15(c) shows the output power and efficiency of the CPT system. In this case, the two coils are separated to eliminate the inductive coupling. Only the metal plates are used to transfer power. When the plates are well aligned, the maximum output power is 0.86 kW with the efficiency of 93.04%. When the plates have 20-cm misalignment, the output power is 0.69 kW, and the efficiency drops to 91.18%.

The output power in Fig. 15(a) is the sum of the output power in Fig. 15(b) and (c), which shows that both the inductive and capacitive coupler can transfer power in the combined system. The capacitive coupler has better misalignment ability when compared to the inductive coupler. When the misalignment

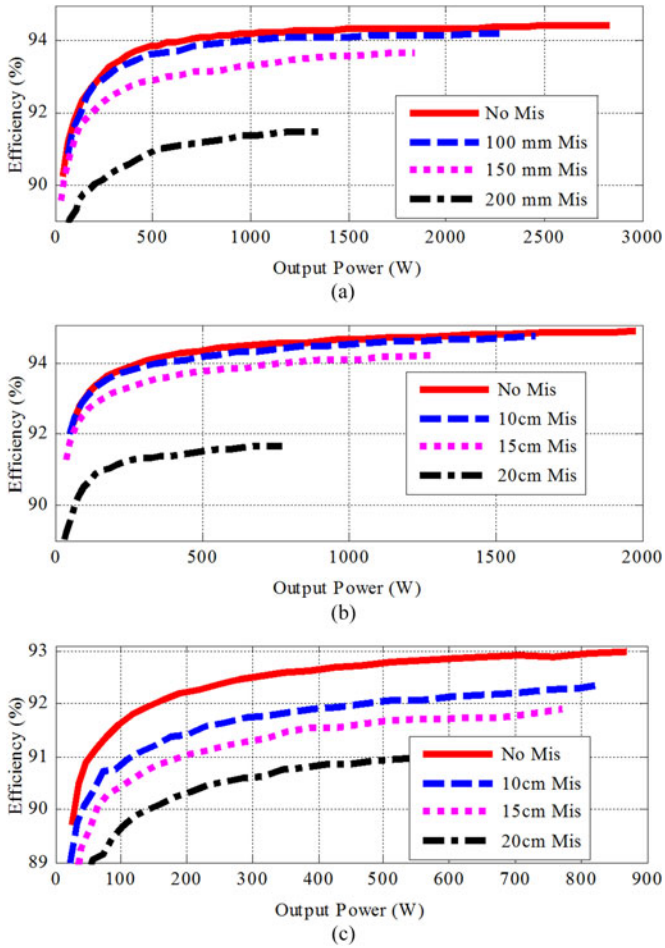

Fig. 15. Measured output power and efficiency for IPT and CPT system. (a) IPT + CPT system. (b) Only IPT system. (c). Only CPT system.

increases to 20 cm, the capacitive coupler can maintain 80.2% of the well-aligned power, and the inductive coupler can only maintain 38.5% of the original power. Therefore, the import of the capacitive coupler to the IPT system can improve the misalignment ability of the system.

C. Comparison of Modeled and Experimental Performance

The experimental performance of the IPT and CPT combined system is compared to the modeled and simulated system in Section IV. The comparisons include the input voltage and current waveforms and the system power and power distribution at different misalignment conditions.

Fig. 16 shows the comparison of the input voltage and current waveforms between the simulated and experimental results, and they agree well with each other. The dashed blue curve is the simulated input voltage, which is a square wave to accelerate calculation speed. The solid red curve is the experimental input voltage, which has a pulse at the switching transient. This is because there is voltage stress on the MOSFETs at the turn-on transient, which can induce some switching losses. However, the magnitude of the pulse is lower than 50 V, so the induced power loss can be neglected. The dashed green curve and solid pink curve are the simulated and experimental input current,

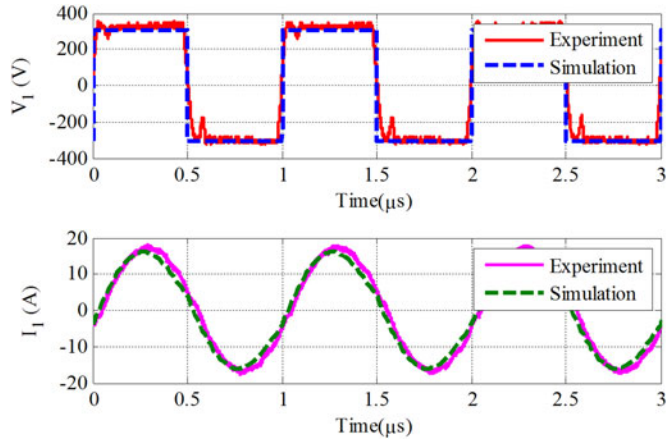

Fig. 16. Comparison of waveforms in simulated and experimental results.

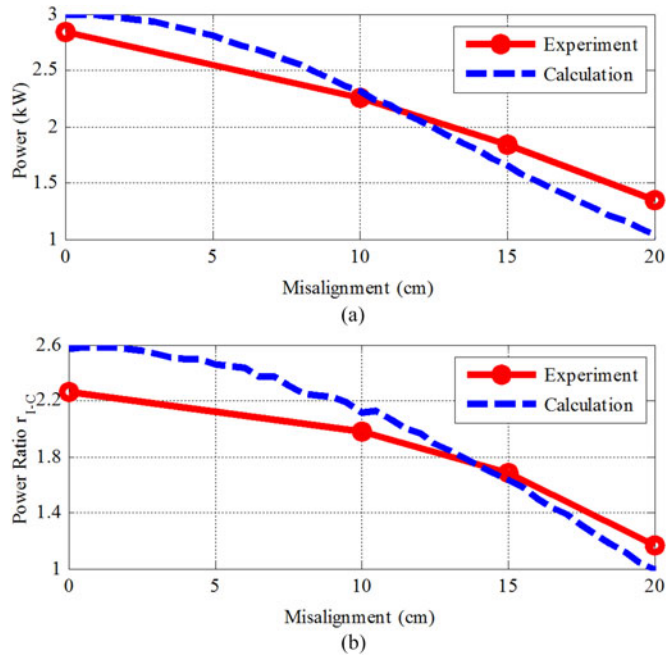

Fig. 17. Comparison of experiment and calculation results. (a) Output power of IPT and CPT combined system. (b) Power ratio between IPT and CPT system.

respectively. The cut off currents of the switching transient are the same.

When there is misalignment, C_s and k decrease as shown in Fig. 10. The FEA analysis shows that the variations of $L_{1,2}$ and $C_{1,2}$ can be neglected. Therefore, (12) and (15) and the parameters in Table I and Fig. 10 are used to calculate the system power at different misalignment conditions. The comparisons of the calculation and experiment results of the system total power and power ratio are shown in Fig. 17.

Fig. 17(a) shows that the calculated and experimental results of the system total power are close at different misalignment conditions. The maximum power difference is within 250 W. When the misalignment is small, the calculation is larger than the experiment result. This is because the calculation does not consider the power losses in the circuit components. When the misalignment increases, the calculation decreases to be lower than the experiment result. This is because the calculation is based on FHA, and all the high-order harmonics currents are neglected. However, with the increase of misalignment, the high-order currents are becoming relatively larger when compared to the fundamental current, so the experiment result is larger than the calculation. It also needs to be emphasized that the difference of power between the calculated and experiment results also increase with misalignment. For example, Fig. 10 shows that, at 20-cm misalignment, the IPT power drops to 25.2%, and the CPT power drops to 62.1%. However, Fig. 15 shows that, in experiments, the IPT power drops to 38.5%, and the CPT power drops to 80.2%. This difference also comes from the approximation of FHA approach. However, the absolute value of the power difference is still in an acceptable range. In future research, the calculation expressions will be modified to consider all the high-order components.

Fig. 17(b) shows the calculated and experimental power ratios between the IPT and CPT system. The maximum ratio difference is within 0.30. When the misalignment increases, both the inductive and capacitive power decreases. The power ratio is also decreasing, which means the capacitive power becomes comparable to the inductive power.

VI. Conclusion

This paper proposes a wireless power transfer system that combines inductive and capacitive power transfer. The innovation is that the inductive coupler and capacitive coupler resonate together, using the compensation components to transfer power. An *LC* compensation topology is required at both the primary and secondary sides. The working principle of the IPT + CPT system is analyzed to derive the expression of the output power and the system design process. The inductive and capacitive couplers are designed using 3-D simulations in Maxwell. A 3.0-kW prototype is constructed to verify the proposed concept. The output power of the combined system is the sum of the IPT and CPT systems. The high voltage between the metal plates is an important safety concern in application. In the future, the system will be optimized to reduce the voltage and the corresponding radiated EMI. Also, the inductive and capacitive coupler can be constructed together to make the system more compact.

References

[1] J. Kim, B. Lee, J. Lee, and S. Lee, "Development of 1 MW inductive power transfer system for a high speed train," *IEEE Trans. Ind. Electron.*, vol. 62, no. 10, pp. 6242–6250, Oct. 2015.

[2] C. Zheng, J. Lai, and L. Zhang, "Design consideration to reduce gap variation and misalignment effects for the inductive power transfer system," *IEEE Trans. Power Electron.*, vol. 30, no. 11, pp. 6108–6119, Nov. 2015.

[3] D. C. Ludois, M. J. Erickson, and J. K. Reed, "Aerodynamic fluid bearing for translational and rotating capacitors in noncontact capacitive power transfer systems," *IEEE Trans. Ind. Appl.*, vol. 50, no. 2, pp. 1025–1033, Mar./Apr. 2014.

[4] J. Dai and D. Ludois, "A survey of wireless power transfer and a critical comparison of inductive and capacitive coupling for small gap applications," *IEEE Trans. Power Electron.*, vol. 30, no. 11, pp. 6017–6029, Nov. 2015.

[5] C. Park, S. Lee, S. Jeong, G. Cho, and C. T. Rim, "Uniform power I-type inductive power transfer system with DQ-power supply rails for

on-line electric vehicles," *IEEE Trans. Power Electron.*, vol. 30, no. 11, pp. 6446–6455, Nov. 2015.
[6] S. Moon, B. Kim, S. Cho, C. Ahn, and G. Moon, "Analysis and design of a wireless power transfer system with an intermediate coil for high efficiency," *IEEE Trans. Ind. Electron.*, vol. 61, no. 11, pp. 5861–5870, Nov. 2014.
[7] J. Kim, D. Kim, and Y. Park, "Analysis of capacitive impedance matching network for simultaneous wireless power transfer to multiple devices," *IEEE Trans. Ind. Electron.*, vol. 62, no. 5, pp. 2807–2813, May 2015.
[8] D. Ahn and S. Hong, "Wireless power transmission with self-regulated output voltage for biomedical implant," *IEEE Trans. Ind. Electron.*, vol. 61, no. 5, pp. 2225–2235, May 2014.
[9] S. Huang, E. Lee, and T. Huang, "Inductive power transfer systems for PT-based ozone-driven circuit with flexible capacity operation and frequency-tracking mechanism," *IEEE Trans. Ind. Electron.*, vol. 61, no. 12, pp. 6691–6699, Dec. 2014.
[10] M. Fu, H. Yin, X. Zhu, and C. Ma, "Analysis and tracking of optimal load in wireless power transfer systems," *IEEE Trans. Power Electron.*, vol. 30, no. 7, pp. 3952–3963, Jul. 2015.
[11] S. Li, W. Li, J. Deng, T. D. Nguyen, and C. Mi, "A double-sided LCC compensation network and its tuning method for wireless power transfer," *IEEE Trans. Veh. Technol.*, vol. 64, no. 6, pp. 2261–2273, Jun. 2015.
[12] J. Deng, F. Lu, S. Li, T. Nguyen, and C. Mi, "Development of a high efficiency primary side controlled 7 kW wireless power charger," in *Proc. IEEE Electr. Veh. Conf.*, Florence, Italy, Dec. 2014, pp. 1–6.
[13] J. Deng, S. Li, S. Hu, C. Mi, and R. Ma, "Design methodology of LLC resonant converters for electric vehicle battery chargers," *IEEE Trans. Veh. Technol.*, vol. 63, no. 4, pp. 1581–1592, May 2014.
[14] J. Deng, W. Li, S. Li, and C. Mi, "Magnetic integration of LCC compensated resonant converter for inductive power transfer applications," in *Proc. IEEE Energy Convers. Congr. Expo.*, Pittsburgh, PA, USA, Sep. 2014, pp. 660–667.
[15] J. Deng, W. Li, T. Nguyen, S. Li, and C. Mi, "Compact and efficient bipolar pads for wireless power chargers: Design and analysis," *IEEE Trans. Power Electron.*, vol. 30, no. 11, pp. 6130–6140, Nov. 2015.
[16] W. Li, C. Mi, S. Li, J. Deng, T. Kan, and H. Zhao, "Integrated LCC compensation topology for wireless charger in electric and plug-in electric vehicle," *IEEE Trans. Ind. Electron.*, vol. 62, no. 7, pp. 4215–4225, Jul. 2015.
[17] D. Shmilovitz, A. Abramovitz, and I. Reichman, "Quasi resonant LED driver with capacitive isolation and high PF," *IEEE J. Emerg. Sel. Topics Power Electron.*, vol. 3, no. 3, pp. 633–641, Sep. 2015.
[18] C. Liu, A. P. Hu, and N. C. Nair, "Coupling study of a rotary capacitive power transfer system," in *Proc. IEEE Int. Ind. Technol. Conf.*, Gippsland, Australia, Feb. 2009, pp. 1–6.
[19] A. P. Hu, C. Liu, and H. Li, "A novel contactless battery charging system for soccer playing robot," *IEEE Int. Mechatron. Mach. Vis. Pract. Conf.*, Auckland, New Zealand, Dec. 2008, pp. 646–650.
[20] H. Funato, H. Kobayashi, and T. Kitabayashi, "Analysis of transfer power of capacitive power transfer system," in *Proc. IEEE Power Electr. Drive Syst.*, Kitakyushu, Japan, Apr. 2013, pp. 1015–1020.
[21] P. Srimuang, N. Puangngernmak, and S. Chalermwisutkul, "13.56 MHz class E power amplifier with 94.6% efficiency and 31 watts output power for RF heating applications," in *Proc. IEEE Electr. Eng. Comp. Telecommun. Inf. Tech. Conf.*, Nakhon Ratchasima, Thailand, May 2014, pp. 1–5.
[22] A. Kumar, S. Pervaiz, C. K. Chang, S. Korhummel, Z. Popovic, and K. K. Afridi, "Investigation of power transfer density enhancement in large air-gap capacitive wireless power transfer system," in *Proc. IEEE Wireless Power Transfer Conf.*, Boulder, CO, USA, May 2015, pp. 1–4.
[23] C. Liu and A. P. Hu, "Power flow control of a capacitively coupled contactless power transfer system," in *Proc. IEEE Ind. Electr. Conf.*, Porto, Portugal, Nov. 2009, pp. 743–747.
[24] M. Kline, I. Izyumin, B. Boser, and S. Sanders, "Capacitive power transfer for contactless charging," in *Proc. IEEE Appl. Power Electr. Conf.*, Fort Worth, TX, USA, Mar. 2011, pp. 1398–1404.
[25] C. Xia, C. Li, and J. Zhang, "Analysis of power transfer characteristic of capacitive power transfer system and inductively coupled power transfer system," in *Proc. IEEE Mech. Sci. Electr. Eng. Comput.*, Jilin, China, Aug. 2011, pp. 1281–1285.
[26] M. P. Theodoridis, "Effective capacitive power transfer," *IEEE Trans. Power Electron.*, vol. 27, no. 12, pp. 4906–4913, Dec. 2012.
[27] B. H. Choi, D. T. Dguyen, S. J. Yoo, J. H. Kim, and C. T. Rim, "A novel source-side monitored capacitive power transfer system for contactless mobile charger using class-E converter," in *Proc. IEEE Veh. Technol. Conf.*, Seoul, Korea, May 2014, pp. 1–5.
[28] L. Huang, A. P. Hu, A. Swwain, and X. Dai, "Comparison of two high frequency converters for capacitive power transfer," in *Proc. IEEE Energy Convers. Congr. Expo.*, Pittsburgh, PA, USA, Sep. 2014, pp. 5437–5443.
[29] T. Kitabayashi, H. Funato, H. Kobayashi, and K. Yamaichi, "Experimental verification of capacitive power transfer using one pulse switching active capacitor for practical use," in *Proc. IEEE Int. Power Electron. Conf.*, Hiroshima, Japan, May 2014, pp. 2517–2522.
[30] J. Dai and D. C. Ludois, "Single active switch power electronics for kilowatt scale capacitive power transfer," *IEEE J. Emerg. Sel. Power Electron.*, vol. 3, no. 1, pp. 315–323, Mar. 2015.
[31] J. Dai and D. C. Ludois, "Capacitive power transfer through a conformal bumper for electric vehicle charging," *IEEE J. Emerg. Sel. Power Electron.*, to be published, doi: 10.1109/JESTPE.2015.2505622
[32] F. Lu, H. Zhang, H. Hofmann, and C. Mi, "A double-sided LCLC-compensated capacitive power transfer system for electric vehicle charging," *IEEE Trans. Power Electron.*, vol. 30, no. 11, pp. 6011–4014, Nov. 2015.
[33] F. Lu, H. Hofmann, J. Deng, and C. Mi, "Output power and efficiency sensitivity to circuit parameter variations in double-sided LCC-compensated wireless power transfer system," in *Proc. IEEE Appl. Power Electr. Conf.*, Charlotte, VA, USA, Mar. 2015, pp. 507–601.
[34] "ICNIRP guidelines for limiting exposure to time-varying electric, magnetic and electromagnetic fields (1 Hz to 100 kHz)," *Health Phys.*, vol. 99, pp. 818–836, 2010.
[35] *IEEE Standard for Safety Levels with Respect to Human Exposure to Radio Frequency Electromagnetic Fields, 3kHz to 300 GHz*, IEEE Standard C95.1, 2005.
[36] F. Lu, H. Zhang, H. Hofmann, and C. Mi, "A high efficiency 3.3 kW loosely-coupled wireless power transfer system without magnetic material," in *Proc. IEEE Energy Convers. Congr. Expo.*, Montreal, Canada, Sep. 2015, pp. 2282–2286.

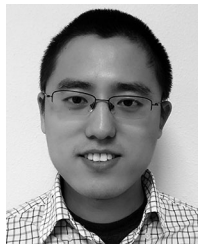

Fei Lu (S'12) received the B.S. and M.S. degrees in electrical engineering from the Harbin Institute of Technology, Harbin, China, in 2010 and 2012, respectively. He is currently working toward the Ph.D. degree in electrical engineering from the University of Michigan, Ann Arbor, MI, USA.

He is working on the high-power and high-efficiency capacitive power transfer through an air-gap distance up to 100's of millimeters. He is also working on the application of widebandgap devices on the WPT system. His research interest includes wireless power transfer for the application of electric vehicle charging.

Hua Zhang (S'14) received the B.S. and M.S. degrees in electrical engineering from Northwestern Polytechnical University, Xi'an, China, in 2011 and 2014, respectively, where she is currently working toward the Ph.D. degree in electrical engineering. From September 2014 to August 2015, she was a joint Ph.D. Student founded by the China Scholarship Council with the University of Michigan, Dearborn, MI, USA.

Since September 2015, she has been with San Diego State University, San Diego, CA, USA. Her research interest includes coupler design of high-power IPT and CPT system.

Heath Hofmann (M'89–SM'15) received the B.S. degree in electrical engineering from The University of Texas at Austin, Austin, TX, USA, in 1992, and the M.S. and Ph.D. degrees in electrical engineering and computer science from the University of California, Berkeley, CA, USA, in 1997 and 1998, respectively.

He is currently an Associate Professor with the University of Michigan, Ann Arbor, MI, USA. His research interests include the design, analysis, and control of electromechanical systems, and power electronics.

Chunting Chris Mi (S'00–M'01–SM'03–F'12) received the B.S.E.E. and M.S.E.E. degrees in electrical engineering from Northwestern Polytechnical University, Xi'an, China, and the Ph.D. degree in electrical engineering from the University of Toronto, Toronto, ON, Canada, in 1985, 1988, and 2001, respectively.

He was with University of Michigan, Dearborn, MI, USA, from 2001 to 2015. He was the President and Chief Technical Officer of 1 Power Solutions, Inc., from 2008 to 2011. He is the Cofounder of Gannon Motors and Controls LLC and Mia Motors, Inc. He is currently a Professor and Chair of electrical and computer engineering and the Director of the Department of Energy—funded Graduate Automotive Technology Education Center for Electric Drive Transportation, San Diego State University, San Diego, CA, USA.

He has conducted extensive research and has published more than 100 journal papers. He has taught tutorials and seminars on the subject of HEVs/PHEVs for the Society of Automotive Engineers, the IEEE, workshops sponsored by the National Science Foundation, and the National Society of Professional Engineers. He has delivered courses to major automotive OEMs and suppliers, including GM, Ford, Chrysler, Honda, Hyundai, Tyco Electronics, A&D Technology, Johnson Controls, Quantum Technology, Delphi, and the European Ph.D. School. He has offered tutorials in many countries, including the U.S., China, Korea, Singapore, Italy, France, and Mexico. He has published more than 100 articles and delivered 30 invited talks and keynote speeches. He has also served as a Panelist in major IEEE and SAE conferences. His research interests include electric drives, power electronics, electric machines, renewable-energy systems, and electrical and hybrid vehicles.

Dr. Mi received the "Distinguished Teaching Award" and the "Distinguished Research Award" of the University of Michigan Dearborn. He also received the 2007 IEEE Region 4 "Outstanding Engineer Award," the "IEEE Southeastern Michigan Section Outstanding Professional Award," and the "SAE Environmental Excellence in Transportation."